J. Fluid Mech. (2025), *vol.* 1016, A22, doi:10.1017/jfm.2025.10407

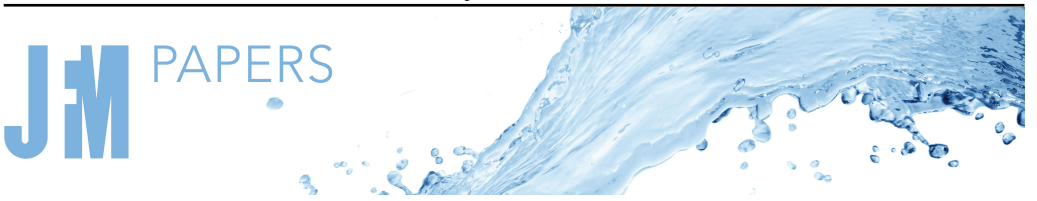

Breakup of viscous liquid bridges on solid surfaces

Salar Farrokhi[1], **Peyman Rostami**[2], **Günter K. Auernhammer**[2] and **Steffen Hardt**[1]

[1]Fachgebiet Nano- und Mikrofluidik, TU Darmstadt, Darmstadt, Germany

[2]Leibniz-Institut für Polymerforschung Dresden e.V., Dresden, Germany

Corresponding author: Steffen Hardt, hardt@nmf.tu-darmstadt.de

(Received 31 July 2024; revised 20 June 2025; accepted 23 June 2025)

The breakup dynamics of viscous liquid bridges on solid surfaces is studied experimentally. It is found that the dynamics bears similarities to the breakup of free liquid bridges in the viscous regime. Nevertheless, the dynamics is significantly influenced by the wettability of the solid substrate. Therefore, it is essential to take into account the interaction between the solid and the liquid, especially at the three-phase contact line. It is shown that when the breakup velocity is low and the solid surface is hydrophobic, the dominant channel of energy dissipation is likely due to thermally activated jumping of molecules, as described by the molecular kinetic theory. Nevertheless, the viscous dissipation in the bulk due to axial flow along the bridge can be of importance for long bridges. In view of this, a scaling relation for the time dependence of the minimum width of the liquid bridge is derived. For high viscosities, the scaling relation captures the time evolution of the minimum width very well. Furthermore, it is found that external geometrical constraints alter the dynamic behaviour of low and high viscosity liquid bridges in a different fashion. This discrepancy is explained by considering the dominant forces in each regime. Lastly, the morphology of the satellite droplets deposited on the surface is qualitatively compared with that of free liquid bridges.

Key words: capillary flows, contact lines, liquid bridges

1. Introduction

The standard scenario of capillary bridge breakup is a liquid bridge spanning the space between two parallel surfaces, here referred to as ‘free liquid bridge’. Over the past

decades, free liquid bridges have been the focus of intense research activities (Kumar 2015; Anthony *et al.* 2023). Three main regimes of liquid bridge breakup have been identified, a viscous regime, an inertial regime and a viscous–inertial regime (Castrejón-Pita *et al.* 2015; Li & Sprittles 2016). In the viscous regime, the dynamics is governed by a balance between capillary and viscous forces, while in the inertial regime, the balance is between capillary and inertial forces. In the viscous–inertial regime, viscous and inertial forces are of equal magnitude. For these different breakup regimes, scaling relationships and similarity solutions have been derived, (see, e.g. Ting & Keller 1990; Eggers 1993; Papageorgiou 1995; Brenner *et al.* 1996; Chen & Steen 1997; Day, Hinch & Lister 1998; Lin 2003; Eggers 2005; Eggers & Villermaux 2008; Eggers 2012*a*,*b*). In the past few years, these studies have been extended to more complex scenarios, e.g. to viscoelastic liquids (Chen *et al.* 2021), to bridges through which an electric current flows (Pan *et al.* 2021; Rubio *et al.* 2021) or to surfactant-laden bridges (Ambravaneswaran & Basaran 1999; Craster, Matar & Papageorgiou 2002; Timmermans & Lister 2002; Liao, Franses & Basaran 2006; McGough & Basaran 2006; Kamat *et al.* 2018; Martínez-Calvo *et al.* 2020; Ponce-Torres *et al.* 2020; Wee *et al.* 2020). Much less attention has been spent on the breakup of liquid bridges that extend along solid surfaces, in the following referred to as 'wetting capillary bridges'. Such structures can be found on surfaces with regions of different wettability. Drop deposition on wettability patterns is relevant for multilayer inkjet printing, where different layers of ink are printed above each other. This technology is used for the fabrication of fuel cells (Towne *et al.* 2007), solar panels (El Mogy 2021) or electric circuits (Kawamoto 2007; Kang, Lee & Oh 2012; Wang *et al.* 2016), among others. When a drop deposited on a wettability pattern evaporates, liquid bridges can be found on a hydrophobic region between two hydrophilic regions (Hartmann & Hardt 2019). When the liquid volume gets reduced by evaporation, a configuration is reached where the Laplace pressure in the liquid bridge can no longer be balanced by the Laplace pressure in the liquid fingers wetting the hydrophilic regions. At this point, an instability is triggered, which was analysed by Hartmann & Hardt (2019) using a parametrised prototypical surface shape. Numerical simulations of the breakup dynamics of water bridges have shown that the process is mainly controlled by a balance between inertial and capillary forces (Hartmann *et al.* 2021). Related to these studies is work that addresses the instability of a liquid ridge on a solid surface based on linear-stability analysis (Davis 1980; Grinfeld 1994; King, Münch & Wagner 2006; Diez & Kondic 2007; Diez, González & Kondic 2009). However, linear-stability theories are not expected to properly account for contact-angle hysteresis, which plays an important role on the vast majority of solid surfaces.

The study on the breakup of wetting capillary bridges presented in this paper relies on the same schemes for analysing data as employed for free liquid bridges. Therefore, subsequently, we briefly introduce these schemes, where we largely follow the analysis of the dynamic regimes presented by Li & Sprittles (2016). When measuring the minimum radius of a free capillary bridge before breakup, usually, curves similar to those shown in figure 1 are obtained. The three different curves represent the inertial, viscous–inertial and viscous regime. At least during a part of the time evolution, the curves align with predictions from similarity solutions, which are essentially different power laws for the different dynamic regimes (Li & Sprittles 2016). It needs to be emphasised that it cannot be expected that the breakup dynamics remains in the same regime during the entire time evolution. Rather than that, transitions between different regimes will occur (Li & Sprittles 2016). For example, when the viscous regime prevails at times relatively long before the point of breakup, a transition to the viscous–inertial regime will occur. However, the transition point may be so close to the point of breakup that the regime transition is hardly measurable or detectable. Apart from the radius of the capillary bridge, the time derivative

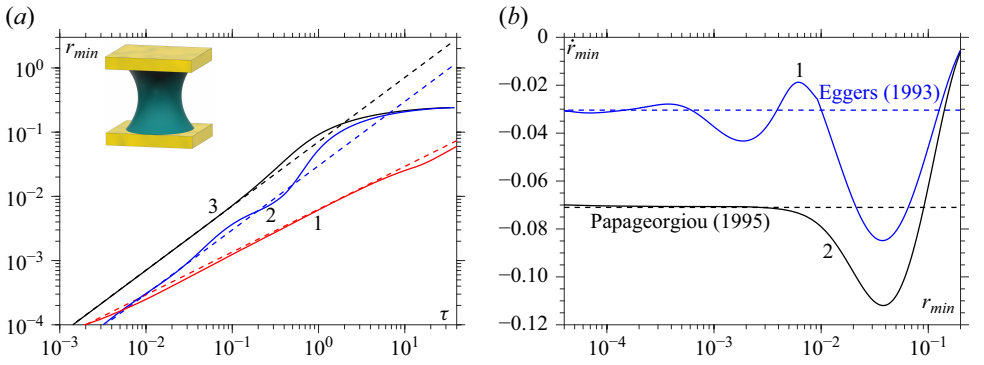

Figure 1. Characteristic time evolution of free liquid bridges before breakup in different regimes. (*a*) Minimum bridge radius against time in the inertial (or $r_{min} \sim \tau^{2/3}$) (1), viscous–inertial (or $r_{min} = 0.0304(\gamma/\eta)\tau$) (2) and viscous (or $r_{min} = 0.0709(\gamma/\eta)\tau$) (3) regime. The dashed lines indicate similarity solutions. (*b*) Breakup speed against minimum bridge radius for the viscous-inertial (1) and the viscous (2) regime. Again, the dashed lines indicate similarity solutions. Reproduced from Li & Sprittles (2016).

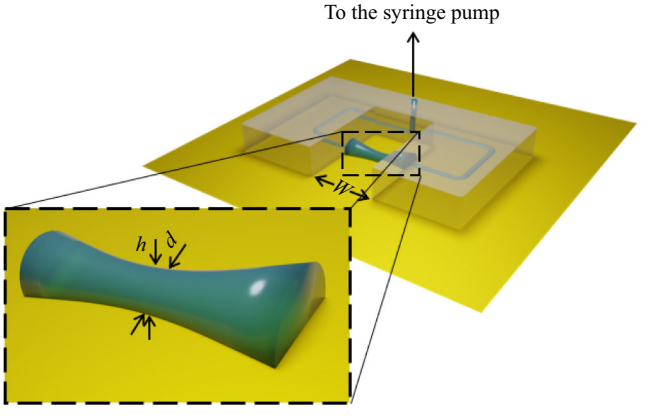

Figure 2. Schematics of the microfluidic set-up and magnified view of the capillary bridge. W is the gap width of the PDMS block, d is the minimum width and h is the minimum height of the capillary bridge.

of the minimum radius, termed 'breakup velocity', is a key quantity characterising the breakup process. Similarity solutions predict a constant breakup velocity for the viscous and viscous–inertial regime (Li & Sprittles 2016) when plotted as a function of the minimum bridge radius, which is exemplified in figure 1(*b*).

In this manuscript, we will use similar methods to characterise the breakup dynamics of viscous wetting capillary bridges. We employ high-speed imaging to study the dynamics of liquids of different viscosities on different surfaces and show that for most liquids, the dynamics follows a viscous scaling law. A marked difference to the breakup dynamics of free liquid bridges lies in the fact that for wetting liquid bridges, a very significant contribution to viscous dissipation is due to the three-phase contact line.

2. Experimental method

2.1. *Microfluidic set-up*

Figure 2 shows the experimental set-up used to create and manipulate the capillary bridge on the substrate. The set-up consists of a polydimethylsiloxane (PDMS) block attached to

a substrate (without plasma treatment of the surface or the PDMS block) and connected to a syringe pump (KDS Legato 200). The PDMS block is fabricated using a standard soft lithography method. After thoroughly mixing the PDMS (Sylgard 184, Dow, Germany) with the corresponding cross-linker in a 10:1 ratio, the mixture is degassed in a desiccator for 1 h to remove the gas bubbles formed during mixing. Subsequently, the mixture is poured onto the three-dimensional (3-D)-printed master structure (Prusa SL1S 3-D printer) and cured in an oven at 40 °C for 24 h. The resulting structure has two channels with a semi-circular cross-section and a diameter of 500 μm. The gap width (W) varies between 0.75 mm and 3 mm.

2.2. *Substrates and liquids*

The substrates are prepared as follows. Silicon wafers (CZ-Si wafer, 4-inch diameter, thickness 500 ± 50 μm, Microchemicals GmbH, Germany) are first coated with a 15 nm layer of chromium and, subsequently, a 50 nm layer of gold using an E-beam method (Balzers BAK 600). Before the coating process, the chamber is preheated to 75 °C and evacuated to a pressure of 6.7×10^{-6} mbar. During the coating, the chamber temperature and pressure are approximately 85 °C and 2×10^{-5} mbar, respectively. To reach coating rates of 0.4 and 0.2 nm s^{-1} for chromium and gold, respectively, 5 kV is applied to evaporate the mentioned materials. The chromium/gold-coated silicon wafers are used as the more hydrophilic substrates. We will refer to this type of surface as 'Au'. The advancing and receding contact angle of water on this surface is 96° and 67°, respectively, determined with a Krüss DSA 100 Drop Shape Analyser. Gold substrates are known to have high surface energy and consequently low contact angles (White 1964; Bewig & Zisman 1965). The main reason for this difference is the contamination of the substrate with impurities. To support our hypothesis, we placed the substrates on a hotplate at 250 °C for 6 min, which reduced the contact angle to 35°. For the rest of this work, we use the chromium/gold coated silicon wafer without any further heat treatment. To achieve more hydrophobicity, a thin PDMS pseudo brush layer is applied to the surfaces. Similar coating processes are detailed elsewhere (Eifert *et al.* 2014), but a brief summary is provided here. First, the surfaces are cleaned in an O_2 plasma chamber (Diener Femto). Next, 0.5 ml of a 5 cSt silicone oil (CAS: 63148-62-9, Sigma–Aldrich, Germany) is dispensed on the surface with a pipette and the surface is pre-heated to 100 °C. After the silicone oil spreads over the entire surface, the surface is placed on a hot-plate at 220 °C for three minutes. Finally, the substrates are rinsed with isopropanol and water for 10 s each. We refer to this type of surface as 'PDMS@Au'. The advancing and receding contact angle of water on this surface is 109° and 95°, respectively, i.e. it is the more hydrophobic one of the two. Since the focus of this study is on viscosity variations, mixtures of water (purified using a Milli-Q device; specific resistance 18.2 MΩ cm at 25 °C) and glycerol (>99.5 %, Sigma–Aldrich, Germany) with different glycerol contents are chosen as the working liquids. The viscosities of the mixtures, measured with a rheometer (Brookfield DV-III Ultra), and the literature values of the surface tension (Takamura, Fischer & Morrow 2012) are presented in table 1, where the percentage represents the mass of glycerol relative to the mass of the mixture. Throughout the remainder of this article, liquids will be referred to by their glycerol percentage.

2.3. *Experimental procedure*

To create the capillary bridge, liquid is pumped through the channels by a syringe pump. The two streams meet on the surface and shape the capillary bridge, after which the pumping is stopped. Next, to bring the capillary bridge to the unstable configuration,

Liquid	Viscosity (mPa s)	Surface tension (mN m^{-1})
0 %	1	71.68
30 %	2.5	70.38
50 %	5.9	69.02
60 %	10.9	68.11
70 %	23.7	66.97

Table 1. Viscosities of the water–glycerol mixtures used in this study as a function of glycerol content.

liquid is withdrawn by the syringe pump. To prevent any bias of the breakup dynamics due to the withdrawal, the withdrawal rate is kept as low as 2 µl min^{-1}. It is known that cured PDMS can contain uncross-linked chains that diffuse to its surface and potentially alter the wetting behaviour (Jensen *et al.* 2015). However, these polymer chains have a very low solubility in aqueous solutions and the results obtained with the current set-up for water closely resemble those from a previous study (Hartmann *et al.* 2021), in which a completely different set-up was used. Therefore, the effect of such polymer chains on the dynamics is marginal. In all experiments, the gold layer is grounded to exclude effects due to slide electrification (Li *et al.* 2022, 2023; Ratschow *et al.* 2024). A coaxial imaging system with a high-speed camera (Photron FASTCAM SA-1.1) in conjunction with 12× macro objective (Navitar) is used to observe the system from the top view. Finally, an in-house MATLAB script with a sub-pixel edge detection method based on a work by Trujillo-Pino *et al.* (2013) with a maximum position error of approximately 0.65 pixels was developed to extract the minimum width of the capillary bridge as well as its breakup velocity from the recorded images. Subject to the required field of view and thus magnification, the pixel resolution varies between 3.66 and 1.57 µm. Depending on the speed of the process, the frame rate was varied between 20 000 and 54 000 frames per second (fps). Due to the limited temporal resolution, it is not possible to determine the breakup time arbitrarily accurately. Therefore, similar to Hartmann *et al.* (2021), the breakup is assumed to occur $\Delta t/2$ s (Δt being the time interval between two consecutive frames) before the first recorded image where the liquid bridge appears to be broken up. The time before breakup is defined as $\tau = t_b - t$, where t_b is the breakup time. For instance, for the first frame where the liquid is broken up, we have $\tau = -\Delta t/2$, whereas in the final recorded image where the liquid bridge remains intact, we have $\tau = \Delta t/2$. In the following sections, the measurements of the minimum width of the liquid bridge as a function of time before breakup will be compared with some power law relations on a logarithmic scale. In these plots, the deviation from the scaling law at small length scales arises from the loss of resolution of the imaging system. While the imaging system is theoretically capable of resolving length scales down to 6 µm, we consistently encountered issues detecting length scales below 7–8 µm. This may be due to the lighting conditions, the image processing code or other parameters. Therefore, less emphasis should be put on the results that show a bridge width below 8 µm.

3. Results

3.1. *Influence of the solid substrate*

This section is dedicated to the effect of substrate wettability on the dynamics of the capillary bridge. To this end, the two surfaces referred to as Au and PDMS@Au are used. Snapshots of the evolution of the capillary bridge for the 60 % liquid on the

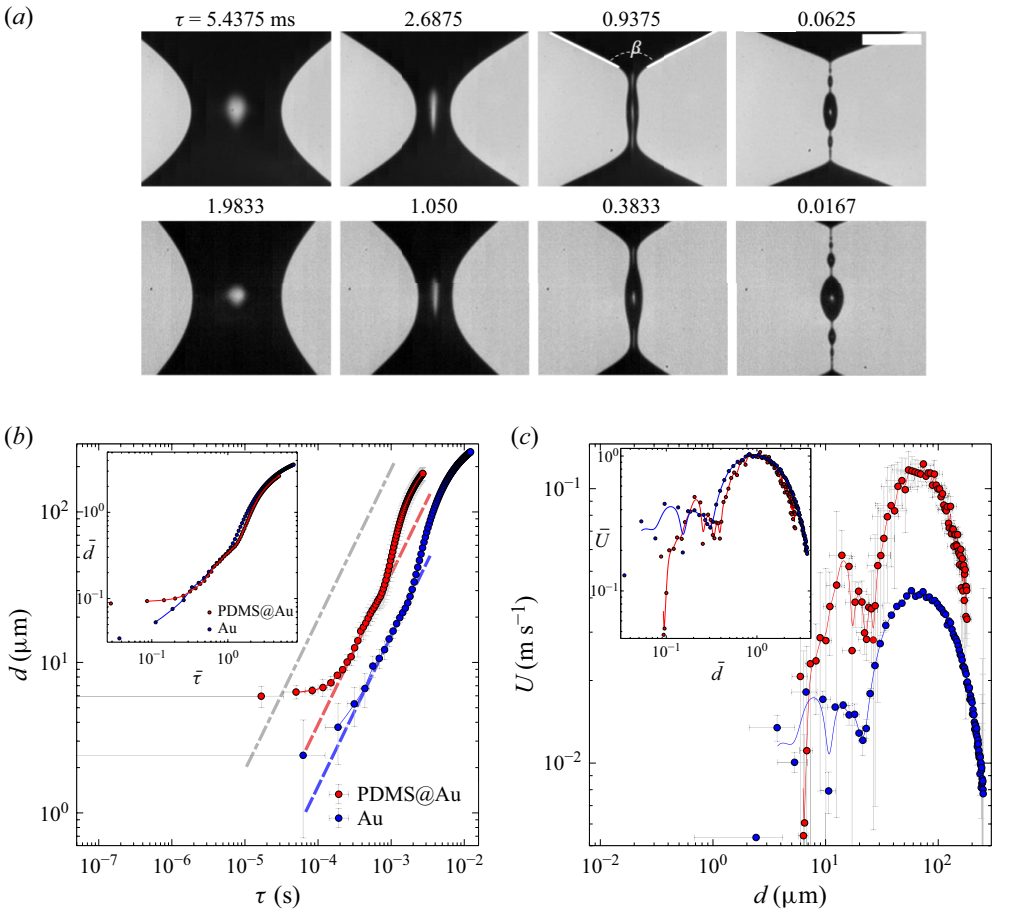

Figure 3. (*a*) Snapshots of the time evolution of the capillary bridge for the 60 % liquid ($Oh = 0.059$) on the Au (top row) and the PDMS@Au (bottom row) surface. τ indicates the time before breakup for each image in ms. The scale bar represents 100 μm. (*b,c*) Influence of the solid substrate on the dynamics of the wetting capillary bridge for the 60 % liquid. (*b*) Minimum width versus time before breakup, (*c*) breakup velocity versus minimum width. The inset in panel (*c*) represents the normalised breakup velocity versus normalised minimum width. The values of the breakup velocity and minimum width at the maxima of each curve are taken for normalisation. The symbols represent measurements, and the solid lines are B-spline fits. The red and blue dashed lines in panel (*b*) represent power laws with a power of one and prefactors of 3.87 and 1.45 cm s^{-1}, and the grey dash-dotted line is the viscous–inertial scaling $r_{min} = 0.0304(\gamma/\eta)\tau$ for a free liquid bridge as a reference. The error bars indicate the standard deviation of at least four experiments. Due to the loss of resolution of the imaging system, less emphasis should be put on $d \leqslant 8$ μm.

aforementioned surfaces are shown in figure 3(*a*). The dark regions correspond to the capillary bridge (with light reflection in the middle), while the brighter regions correspond to the solid surface. The frames are selected in a way that the minimum width of the bridges (d) for the two cases in each column is equal. This implies that the time before breakup τ (see § 2.2) is different for two corresponding frames in the top and bottom rows. For example, the first frame for the PDMS@Au case corresponds to approximately 1.98 ms before breakup, whereas that of the Au case corresponds to approximately 5.44 ms. It should be noted that the position of the minimum width during breakup shifts. This point will be further discussed in § 3.4.

Clearly, the two cases exhibit differences in shape, such as the cone opening angle (β) and the axial elongation of the capillary bridge. These differences are also visible in the d versus τ and U ($= \mathrm{d}d/\mathrm{d}\tau$) versus d data, see figures 3(b) and 3(c). The symbols represent measurements and the solid lines depict B-spline fits to the data points. In this and in some of the following figures, the B-spline fits merely serve as guides to the eye. As shown in figure 3, qualitatively, in each case, the dynamic behaviour is very similar to the dynamic behaviour of highly viscous free capillary bridges (Papageorgiou 1995; Li & Sprittles 2016*b*) as indicated by the convergence of the curves to the power laws with a power of one (the dashed lines). However, there is a substantial dependence of the dynamics on surface properties. For instance, the breakup velocity on the PDMS@Au (more hydrophobic) surface is much higher (approximately three times higher on average) than on the Au surface. It should be mentioned that a similar behaviour – namely, faster breakup dynamics on PDMS@Au surfaces – is also observed with other liquids (data not shown). Therefore, it can be inferred that the more hydrophobic surface imposes less resistance on the motion of the capillary bridge than the Au surface, leading to higher velocity and greater elongation in the axial direction for the former case. The dependence of the dynamics on the wetting properties implies that the solid–liquid interaction, especially at the three-phase contact line, must be taken into account to understand the dynamics of capillary breakup of viscous liquids on solid surfaces.

Despite the clear effect of the solid substrate on the breakup velocity, we provide a brief comparison between the breakup dynamics of wetting and free liquid bridges as a reference. It has been shown that the breakup dynamics of a free liquid bridge is primarily governed by the non-dimensional Ohnesorge number, $Oh = \eta/\sqrt{\rho\gamma a^*}$; where ρ, γ, a^* are density, surface tension and a characteristic length scale of the problem, respectively (Castrejón-Pita *et al.* 2015; Li & Sprittles 2016). For the 60 % liquid used in this study, taking the diameter of the channel as the characteristic length scale, we obtain $Oh = 0.059$. At such Ohnesorge numbers, a free liquid bridge is expected to be predominantly in the viscous–inertial regime near pinch-off (Castrejón-Pita *et al.* 2015; Li & Sprittles 2016). Therefore, we compare our results with the universal viscous–inertial scaling, namely $r_{min} = 0.0304(\gamma/\eta)\tau$. As can be seen in figure 3(b), the grey dash-dotted line, which represents the viscous–inertial scaling, lies significantly to the left of the experimental data. This indicates that the capillary breakup occurs much more slowly for wetting liquid bridges compared to free liquid bridges – approximately five times slower for the PDMS@Au and 13 times slower for the Au surface. As noted earlier in this section, contact line forces contribute significantly to the resistive forces in wetting liquid bridges. Therefore, the much faster capillary breakup observed for free liquid bridges, where such forces are absent, is expected.

3.2. *Influence of viscosity*

To clarify the influence of viscosity on the dynamic behaviour of the capillary bridge on the solid surfaces, five different water–glycerol mixtures were used in the experiments. Figure 4 depicts the time evolution of the capillary bridge for the 0 % and 70 % liquids. The frames are selected in a way that the minimum width of the bridges (d) for the two cases in each column is comparable. All experiments were conducted on the PDMS@Au surface. It is worth noting that, in comparison to the viscosity variations, the wetting behaviour of the working liquids on the PDMS@Au surface shows minimal variation. For instance, the advancing and receding contact angles for the 70 % liquid are approximately 101° and 88°, respectively (for comparison with water, see § 2.2). Consequently, in the following discussion, we will attribute the observed changes in dynamics to the viscosity

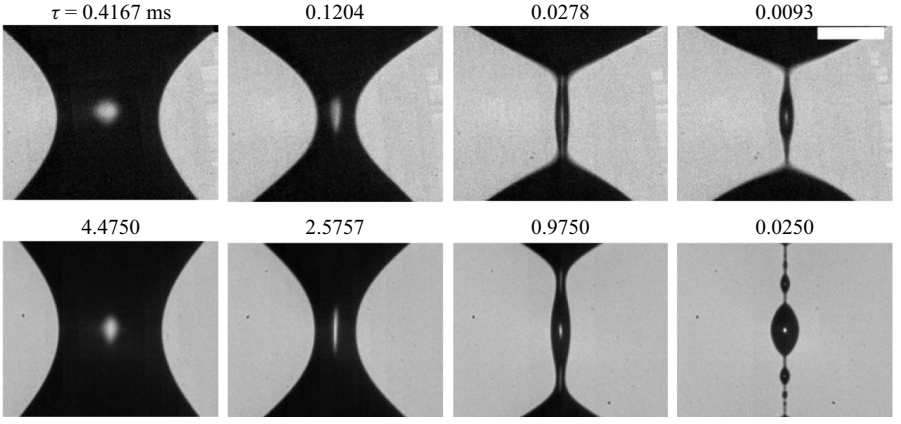

Figure 4. Snapshots of the time evolution of the capillary bridge for the 0 % liquid ($Oh = 0.005$), in the top row, and the 70 % liquid ($Oh = 0.129$), in the bottom row, on the PDMS@Au surface. τ indicates the time before breakup for each image in ms. The scale bar represents 100 µm.

variations. As can be seen in the snapshots, the more viscous liquid bridge has a larger axial elongation, as well as a smaller cone opening angle.

Figure 5(*a*) shows the d versus τ plots for various viscosities. The symbols represent measurements and the solid lines are B-spline fits to the data points. The dashed lines represent a power law with a power of one, whose relevance will be further discussed in this section (for more details, see § 3.2.2). It can be seen that the dynamics of the 50–70 % liquids look very similar, the curves are merely shifted along the x-axis. Keeping in mind that figure 5(*a*) is a log–log plot, the horizontal shift of the curves represents a change in the velocity ($U = (\mathrm{d}d/\mathrm{d}\tau)$). In other words, by increasing the viscosity, the breakup process slows down. It should be mentioned that the breakup dynamics for the case of low viscosity liquids (e.g. water) has been investigated by Hartmann *et al.* (2021). In that study, it was concluded that the dynamics follows an inertial scaling $d \sim \tau^{2/3}$ in an average sense. This is also confirmed in the present study, indicated by the fact that the red dotted line has a slope of 2/3. Considering the similar qualitative behaviour of highly viscous free and wetting capillary bridges, one might be tempted to assume the viscous scaling for the free capillary bridge to be valid for the capillary bridge on a solid substrate. However, as already noted in § 3.1, the scaling for the latter must take into account the wetting properties of the surface.

3.2.1. *Dominating sources of dissipation*

The motion of a three-phase contact line is an irreversible process, resulting in energy dissipation (Huh & Scriven 1971; De Gennes 1985; Blake 2006).

There are two common ways of describing the energy dissipation at moving contact lines: the so-called hydrodynamic theory and the molecular kinetic theory (MKT). The hydrodynamic theory considers the viscous dissipation in the wedge near the contact line based on the Navier–Stokes equation (Voinov 1976; Bonn *et al.* 2009). Since this dissipation is a function of the wedge angle (dynamic contact angle), surface wettability enters the equations. It has been shown that (Bonn *et al.* 2009)

$$D_{hyd} \approx \eta U^2 \frac{\ln\left(\frac{R_0}{R_i}\right)}{\theta_D} L, \tag{3.1}$$

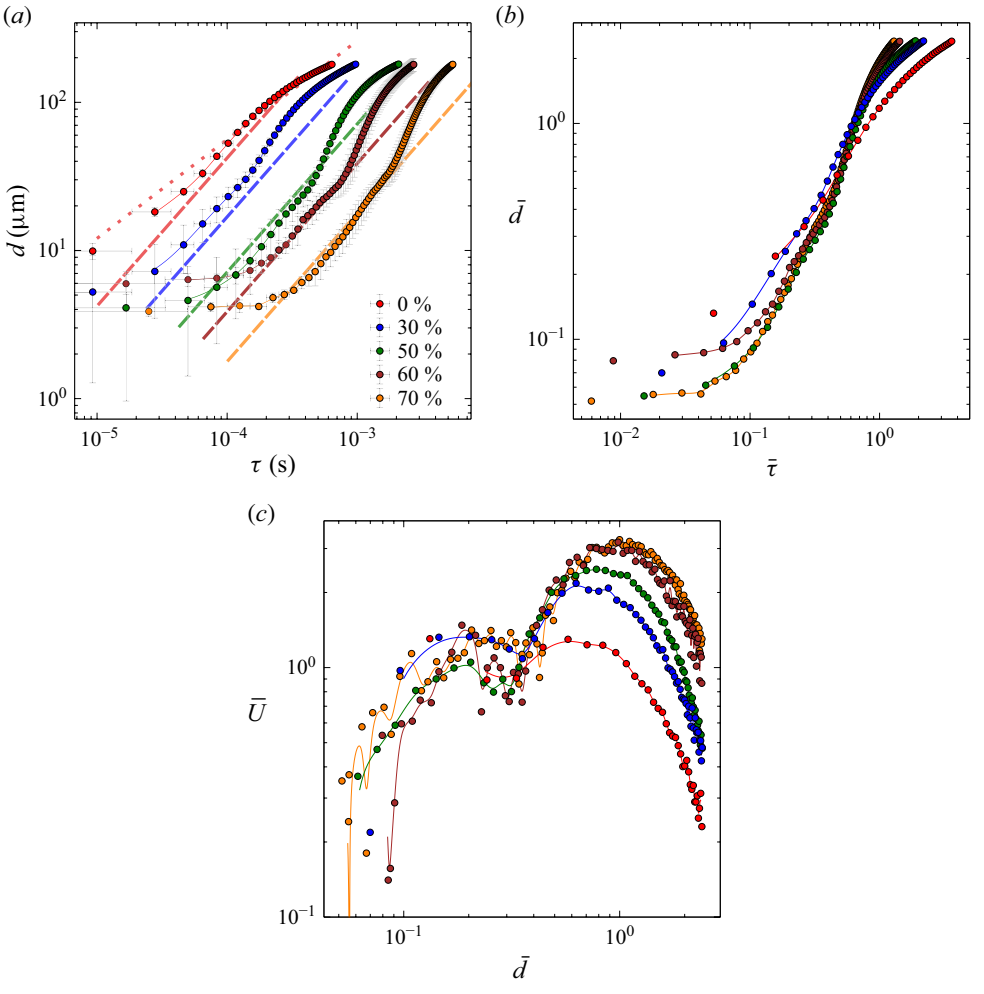

Figure 5. Influence of viscosity on the dynamics of the capillary bridge on the PDMS@Au surface ($Oh = 0.005-0.12$.) (*a*) Minimum width versus time before breakup. The dashed lines represent power laws with a power of one, where the prefactor for the 70 % liquid is 1.78 cm s^{-1}, and the prefactors for the remaining cases are calculated accordingly (see § 3.2.2). The error bars represent the standard deviation of at least four experiments. (*b*) Scaled minimum width versus scaled time before breakup. The minimum width is normalised with the minimum width at maximum velocity of the 70 % (a_m) liquid. The time before breakup is normalised with $\zeta_{tot} a_m/\gamma$. (*c*) Scaled breakup velocity versus scaled minimum width. The breakup velocity is scaled with γ/ζ_{tot}. The legend of panel (*a*) applies to all panels. Due to the loss of resolution of the imaging system, less emphasis should be put on $d \leqslant 8\,\mu$m.

where D_{hyd} is the dissipated power according to the hydrodynamic theory, η is the liquid viscosity, U is the contact line velocity, R_i is a microscopic cut-off length, R_0 is a macroscopic length scale (drop radius, for example), θ_D is the dynamic contact angle and L is the length of the contact line. It should be noted that in the literature, the energy dissipation at the contact line is often considered per unit length of the contact line (see, e.g. Bonn *et al.* 2009). However, in view of the scaling relation at which we are aiming, the total energy dissipation over the entire length of the contact line is considered here. In contrast to the hydrodynamic theory, the MKT neglects the hydrodynamic viscous dissipation altogether and introduces a molecular mechanism for the dissipation at the

contact line (Blake & De Coninck 2002). According to this theory, molecular motion in the vicinity of the contact line is the dominant channel of dissipation. It has been shown that the contact line velocity is related to the contact angle through the following relation:

$$U = 2\kappa^0 \lambda \sinh\left(\gamma \lambda^2 \frac{\cos(\theta_S) - \cos(\theta_D)}{2k_B T}\right), \tag{3.2}$$

where U is the contact line velocity, κ^0 is the frequency at which molecular jumps occur at equilibrium, λ is the jump length, γ is the surface tension, θ_S and θ_D are the static and dynamic values of the contact angle, k_B is the Boltzmann constant, and T is the absolute temperature. If the argument of the sinh function is not too large, that is, the contact angle does not significantly deviate from its static value, this equation can be linearised to the following:

$$U = \frac{\gamma}{\zeta}(\cos(\theta_S) - \cos(\theta_D)), \tag{3.3}$$

where $\zeta = k_B T/\kappa^0 \lambda^3$. It should be noted that for a given surface at constant temperature, this factor is constant and is denoted as 'contact line friction'. It has been shown that contact line friction can be related to the static contact angle as well as viscosity through the following equation (Blake & De Coninck 2002; Blake 2006):

$$\zeta = \eta\left(\frac{v_L}{\lambda^3}\right)\exp\left(\frac{\lambda^2 Wa}{k_B T}\right), \tag{3.4}$$

where v_L is the volume of unit flow, which for many simple liquids is equal to the molecular volume, and $Wa = 1 + \cos(\theta_S)$ is the work of adhesion (Blake & De Coninck 2002). Intuitively, increasing the liquid viscosity or reducing the hydrophobicity of the surface would increase the dissipation at the contact line.

Re-arranging the terms in (3.3), it can be inferred that the surface force $\gamma(\cos(\theta_S - \cos(\theta_D))$ on the contact line that is obtained by considering the force balance on a control volume is equal to the friction force on the contact line ζU; hence, the term 'contact line friction'. Therefore, the dissipated power of the contact line through this mechanism can be written as

$$D_{MKT} = \zeta U^2 L. \tag{3.5}$$

Both the hydrodynamic theory and the MKT have been successful in describing dynamic wetting phenomena (Blake 2006). In realistic scenarios, it is plausible that dissipation is a combination of both mechanisms. However, one can identify the dominant source of dissipation relevant to a specific problem. According to (3.1) and (3.5),

$$\frac{D_{hyd}}{D_{MKT}} = \frac{\eta \cdot U^2 \cdot \ln\left(\frac{R_o}{R_i}\right)/\theta_D \cdot L}{\zeta \cdot U^2 \cdot L}. \tag{3.6}$$

For the PDMS@Au surface, the receding contact angle is $\theta_{rec} \approx 96°$. Assuming that the contact line velocity while receding is not too large, which is the case for highly viscous capillary bridges, $\theta_D \approx \pi/2$ is a reasonable estimate. Furthermore, on average, the ratio of viscosity and contact line friction is $\eta/\zeta \approx 80$ (Duvivier *et al.* 2013). Finally, assuming $\ln(R_o/R_i) \approx 10$, a typical value from the literature (Blake 2006), we obtain

$$\frac{D_{hyd}}{D_{MKT}} \approx 0.1. \tag{3.7}$$

Therefore, it can be concluded that for such scenarios of wetting liquid bridges, i.e. rather slowly moving contact lines and hydrophobic surfaces, the dominant source of dissipation is most likely that of the MKT. However, in the following, we attempt to treat the hydrodynamic theory and the MKT on an equal footing, using an approximate description. The hydrodynamic theory and the MKT suggest different relations between the dynamic contact angle and the contact line velocity. For example, in the simplified case of small contact angles, according to the hydrodynamic theory (Voinov 2000; Bonn *et al.* 2009):

$$\theta_D^3 = \theta_m^3 + A \cdot Ca, \tag{3.8}$$

and the MKT (Blake 2006):

$$\theta_D^2 = \theta_S^2 + B \cdot Ca, \tag{3.9}$$

where θ_m is the microscopic contact angle, A and B are some constants, and $Ca = \eta U/\gamma$ is the capillary number. Despite the differences in the scaling of the dynamic contact angle with Ca, a zeroth-order approximation for small capillary numbers yields a constant value for the contact angle. In other words, for small Ca numbers, we neglect the dependence of the dynamic contact angle on velocity. Taking $\theta_D \approx$ const., D_{hyd} also scales as U^2. Therefore, we can combine the hydrodynamic wedge dissipation and the dissipation according to the MKT, introducing an effective contact line friction factor ζ_{CL},

$$D_{CL} = \zeta_{CL} U^2 L, \tag{3.10}$$

where the subscript CL stands for contact line. Since, according to the estimate of (3.7), the energy dissipation according to the MKT is much larger than the hydrodynamic dissipation in the liquid wedge, the error due to considering a constant value for θ_D is minor. This means that even beyond the regime of small capillary numbers, the scaling of (3.10) is very likely a good approximation. Furthermore, it should be mentioned that (3.2) has been derived for hard substrates. Nevertheless, it has been shown that the dissipation on PDMS pseudo-brushes also scales as U^2 (Rostami *et al.* 2023). Therefore, the corresponding dissipation can also be included in the effective contact line friction.

It is also necessary to identify other sources of dissipation and compare their magnitude to the energy dissipation at the three-phase contact line. It can be shown that the dissipation according to the MKT is much larger than the viscous dissipation due to the radial flow in the bulk of the liquid. In that context, the term 'radial flow' refers to the flow in the direction of contact-line motion. The corresponding shear stress on the solid surface can be approximated by $\eta U/h$, which acts on an area of approximately $d \cdot L$, where h represents the minimum height of the liquid bridge. Thus, the ratio of the viscous dissipation in the bulk due to the radial flow (D_{rad}) and the dissipation according to the MKT (D_{MKT}) can be written as follows:

$$\frac{D_{rad}}{D_{MKT}} \approx \frac{\eta \cdot U^2/h \cdot d \cdot L}{\zeta \cdot U^2 \cdot L}. \tag{3.11}$$

Substituting the aforementioned values and considering the fact that for the surface used in this study at low contact line velocities $\theta_D \approx \pi/2$, or in other words, $h \sim d$, this ratio would be approximately 0.012. Therefore, it can be concluded that viscous dissipation in the bulk due to the radial flow is only of minor importance.

To complete the picture, the viscous dissipation in the bulk due to the axial flow (D_{ax}) needs to be estimated. Here, the term 'axial flow' refers to the flow in the direction along which the liquid bridge extends. Similar to the previous analysis for the radial direction,

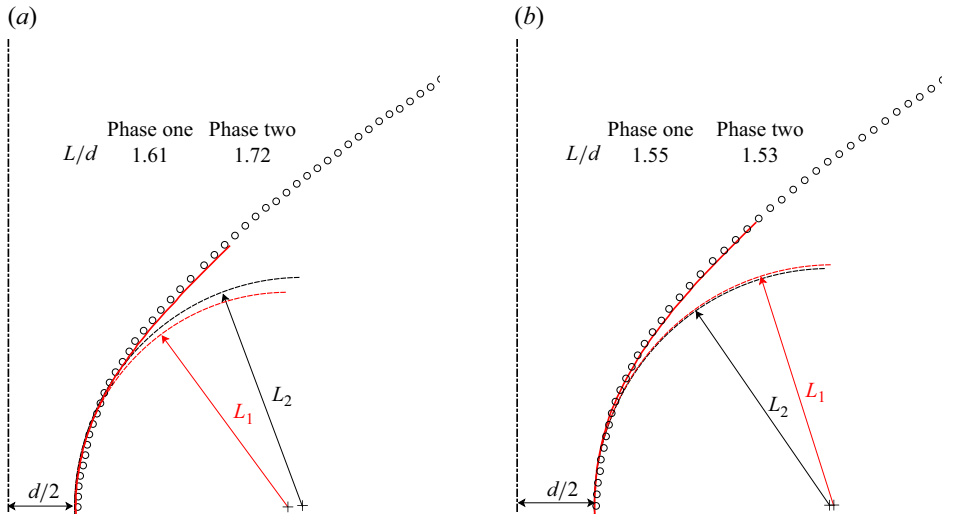

Figure 6. Scaled profiles of the contact line in phase one (red curves) and corresponding instants in phase two (open circle symbols) for (*a*) the 60 % and (*b*) the 70 % liquid, obtained from high-speed images. The experiments were done on the PDMS@Au surface. The profiles represents the instant in which the velocity is maximum in each phase. The dashed lines represent the osculating circle at the location of minimum width.

it can be shown that $D_{ax} \approx \eta \cdot U_z^2/h \cdot d \cdot L$, where U_z is some characteristic flow velocity in the axial direction. Taking the length of the contact line as an axial length scale and assuming U to be a typical velocity in the radial direction, from the continuity equation, it can be shown that $U_z \sim (L/\mathrm{d})U$. Therefore,

$$D_{ax} \approx \left(\frac{L}{d}\right)^2 \eta U^2 L. \tag{3.12}$$

The value L/d is a geometric factor representing the slenderness of the liquid bridge. This ratio is a function of the surface wettability, liquid viscosity and time. It should be noted that determining L, and consequently L/d, is not straightforward, as the region of interest for capillary breakup is not immediately apparent from the experimental images. Therefore, we define L as the radius of curvature of the contact line at the location of minimum width.

Despite the intricate dependency of L/d on different parameters, if one considers the average over a broader time interval, this value remains approximately constant for a given liquid and substrate. This is due to undulation of the surface of the liquid bridge. When the capillary breakup begins, the minimum width of the bridge is in the middle. We call this period phase one. After some time has elapsed, the position of minimum width shifts to the two ends, creating two symmetrical necks and a bulge in the middle. We call this phase two. This phenomenon recurs and gives rise to multiple necks. The subsequent necks are geometrically similar to those in phase one. This can be made clear by comparing the profiles of the contact lines in the corresponding phases of the time evolution. Figure 6 depicts the scaled profiles of the contact line in the constricted part of the liquid bridge in phase one (red curves) with the profiles at the equivalent instant in phase two (open circle symbols) for two different liquids on the PDMS@Au surface. The corresponding experiments are shown in figures 3 and 4. The dashed lines represent the osculating circles at the location of minimum width, whose radii are denoted as L_1 and L_2. It should be

noted that in phase one, the liquid bridge is symmetric and connected to the so-called 'reservoirs' at both ends. In contrast, in phase two, this symmetry is lost: on one side, the necks are connected to the reservoirs, while on the other side, they are connected to the central bulge. As a result, geometric similarity between the contact line profiles of phases one and two is only expected in the region where the boundary conditions are comparable. Specifically, only the contact line profile between the location of minimum width and the reservoir is shown for both phases. The profile from phase one is scaled according to the ratio of minimum widths d_1/d_2 to match the minimum width of phase two. As can be seen in figure 6, the red curves align very well with the symbols, and the ratio L/d remains approximately constant.

As can be seen, the profile of the contact lines aligns reasonably well. A quantitative comparison of L/d is presented in figure 6. Thus, due to the geometric similarity between different phases, L/d is constant when averaged over a longer time interval, leading to $D_{ax} \sim U^2$. Therefore, the resulting dissipation due to all aforementioned channels can be summarised in the following equation by introducing a total friction factor ζ_{tot}:

$$D_{tot} = \zeta_{tot} U^2 L. \tag{3.13}$$

Throughout this paper, we will refer to the combined effects of the mentioned mechanisms as the friction force. Nevertheless, it is helpful to know in which part of the parameter space which dissipation mechanism tends to dominate. In our experiments, we observed that by increasing the viscosity of the liquid or the contact angle of the surface, L/d increases. The maximum value of L/d (3.5) corresponds to the breakup of the 70 % liquid on the PDMS@Au surface, and the minimum value (1.9) corresponds to the 0 % liquid on the Au surface. It should be noted that many parameters such as surface roughness and contact angle hysteresis influence the wetting properties, and consequently the capillary breakup dynamics. However, to provide a simple characterisation of the dominating dissipation mechanism, here, we only consider the contact angle. Then, the following qualitative statement can be made: for surfaces with smaller contact angle or liquids with lower viscosity, the major contribution to the total friction factor stems from contact line effects.

3.2.2. *Scaling arguments*

In the remainder of this section, a scaling relation is derived by considering the friction force and the capillary force. Considering the capillary bridge to be a slender thread, the curvature of the liquid surface is $\kappa \sim 1/h$, see the zoomed-in image in figure 2. The Laplace pressure due to this curvature, acting on an area A, balances the friction force:

$$\gamma \cdot \kappa \cdot A \sim \zeta_{tot} \cdot U \cdot L, \tag{3.14}$$

where U is a typical velocity in the radial direction. By taking $U \sim d/\tau$ and $A \sim h \cdot L$, the force balance reduces to

$$d \sim \frac{\gamma}{\zeta_{tot}} \tau. \tag{3.15}$$

Equation (3.15) is reminiscent of the well-known viscous law for the free capillary bridge, and this resemblance explains the similar qualitative behaviour in the d versus τ diagrams. In the remainder of this paper, we will refer to the dynamic regime that follows the scaling of (3.15) as the viscous regime. In figure 5(*a*), the dashed lines represent the asymptotes $d \sim \tau$, obtained as follows: first, a power law with a power of 1 is fitted to the 70 % liquid in the region $6\,\mu\text{m} < d < 40\,\mu\text{m}$. Then, the rest of the fit functions (dashed

lines) are calculated by considering the viscosity dependence of the friction factor $\zeta_{tot} \sim \eta$. It should be noted that the intricate dependence of ζ_{tot} on surface tension was neglected when computing these fit functions, i.e. only the viscosity dependence was considered. The lower bound of d in curve fitting is chosen according to the optical resolution of the imaging system, while the upper bound corresponds to the time where the liquid bridge of roughly uniform width appears. In the context of the capillary breakup of free liquid bridges, it has been established that the entrance to the viscous scaling regime is a function of the geometry of the system or the shape of the liquid bridge and independent of the viscosity of the liquid (Li & Sprittles 2016). We have observed a similar behaviour for the wetting liquid bridges. This is verified by the fact that for the liquids that follow the scaling fairly well, namely the 50 %–70 % liquids, the power-law behaviour starts at $d \approx 40\,\mu$m. Nevertheless, deviations occur for the 30 % liquid, which can be attributed to the increasing importance of inertia at higher velocities. Figure 5(*b*) shows the scaled minimum width ($\overline{d}$) versus scaled time before breakup ($\overline{\tau}$). Here, the bridge width is scaled by dividing by some length scale a_m, and time is scaled with $\zeta_{tot} a_m/\gamma$. Furthermore, a physically meaningful length scale will be introduced in § 3.3. For the moment, the length scale is arbitrarily chosen to be 75 μm (the minimum width where the 70 % liquid has the maximum velocity). A natural velocity scale for the problem is $U^* = \gamma/\zeta_{tot}$, which is similar to the intrinsic capillary velocity (γ/η). Figure 5(*c*) shows the scaled breakup velocity (U/U^*) as a function of the scaled minimum width of the capillary bridge.

3.3. *Influence of geometric constraints*

By altering the gap width (W in figure 1) of the PDMS block, the effect of external length scales on the breakup dynamics can be studied. To achieve this, experiments have been conducted with three different gap widths: 3, 1.5 and 0.75 mm, denoted as L, M and S, respectively. U versus d plots for the 70 % and 0 % liquids can be found in figures 7(*a*) and 7(*c*), respectively. The key difference between the plots is the fact that by decreasing the size of the system, there is a significant increase in the maximum breakup velocity for the 0 % liquid, whereas for the 70 % liquid, there is only a shift along the x-axis and no apparent change in the maximum velocity, see figures 7(*a*) and 7(*c*). This difference can be explained by considering the forces at play in each regime. For the 0 % liquid (inertial regime), capillary forces are balanced by inertial forces, while for the 70 % liquid (viscous regime), they are balanced by friction forces. Typical time ($\hat{t}$), length ($\hat{d}$) and velocity scales ($\hat{V}$) for each of these regimes can be written as follows:

$$\hat{t}_v = \frac{\zeta_{tot} a}{\gamma}, \quad \hat{d} = a \Rightarrow \hat{V}_v = \frac{\gamma}{\zeta_{tot}}, \tag{3.16}$$

$$\hat{t}_i = \left(\frac{\rho a^3}{\gamma}\right)^{0.5}, \quad \hat{d} = a \Rightarrow \hat{V}_i = \left(\frac{\gamma}{\rho a}\right)^{0.5}, \tag{3.17}$$

where ρ is the mass density, a is a characteristic length scale, and the subscripts i and v indicate the inertial and viscous regimes, respectively. Evidently, in the viscous regime, the characteristic velocity remains independent of any length scale, while in the inertial regime, the velocity scales inversely with the square root of the length scale. The fact that by increasing the size, the dynamics slows down should not be surprising for inertial dynamics.

To proceed, we need to identify the characteristic length scale a, which can depend on the geometric scales of the problem, but also on combinations of other problem parameters

with the dimension of a length. For the latter, the capillary length could come into play, but can be ruled out because of the negligible relevance of gravitational forces on sub-millimetre scales. With respect to the geometric scales, in addition to the gap width, other scales such as the channel width could potentially influence the dynamics of the capillary bridge. Therefore, the relationship between W and a is not immediately clear. However, in any case, there is a minimum width of the capillary bridge where the bridge becomes unstable. This minimum width is called a_{crit}. Capillary bridges formed under different geometric constraints but in the same dynamic regime are expected to follow a universal dynamic behaviour. In other words, with the correct scaling, the corresponding curves in the U versus d space should collapse onto a master curve. Since by definition a_{crit} indicates the starting point of the instability, one can hypothesise that choosing $a = a_{crit}$ and the velocity scales of (3.16) and (3.17) would result in a collapse of curves. However, determining a_{crit} proves to be challenging. To eliminate these complications, the width of the capillary bridge at the maximum velocity (a_{max}) is taken as the length scale. Figure 7(b) shows an excellent collapse of curves for the 70 % liquid based on this length scale. It can be seen in the U versus d curves that the onset of instability for highly viscous liquids occurs approximately at $3a_{max}$, which indicates that, to a reasonable approximation, there is a fixed relationship between a_{crit} and a_{max}. Correspondingly, the scalings with a_{crit} and a_{max} appear to be equivalent.

3.4. *Formation of satellite droplets*

The purpose of this section is to qualitatively compare the morphologies of the final configurations after liquid-bridge breakup as observed for free and wetting liquid bridges. As can be seen in figure 3(a) and figure 4, and as discussed before, the position of the minimum width of a capillary bridge does not always remain in the middle; instead, it shifts towards the two ends. This phenomenon occurs repeatedly, leading to the formation of several necks in the liquid bridge and, consequently, the generation of multiple satellite droplets (Tomotika 1935; Tjahjadi, Stone & Ottino 1992; Bhat *et al.* 2010; Peschka *et al.* 2019). Here, we will refer to this recursive phenomenon as higher order necking. Reports on satellite droplet formation for wetting liquid bridges are rare, the work by Peschka *et al.* (2019) being one exception. The authors attributed the changes in the satellite droplet configuration to dissipation at the contact line, which they modelled using an effective Navier slip length. These findings indicate the suppression of satellite formation for intermediate slip lengths. While this sheds light on the breakup of liquid threads on solid surfaces, the findings are only of limited relevance for our work. This is because in experiments, it is difficult to vary the slip length over a significant range, and a variation of the slip length usually yields a modification of other parameters such as the contact angle as well.

For a free capillary bridge surrounded by an inviscid fluid, the following behaviour is observed in the high- and low-viscosity limit. In viscous dynamics, capillary bridges tend to form an elongated thread where the minimum radius remains in the middle for a long time, whereas bridges of low viscosity soon tend to develop secondary necks close to the two ends, resulting in a comparatively large satellite droplet in the middle. For highly viscous liquids, viscous dynamics describes the dynamic behaviour throughout most of capillary breakup. However, the final stage of the breakup occurs in the viscous–inertial regime (Li & Sprittles 2016). In the viscous–inertial regime of capillary breakup, there is a small satellite droplet in the middle of the bridge, with two thin threads on either side. Much less attention has been paid to the higher order necking and satellite

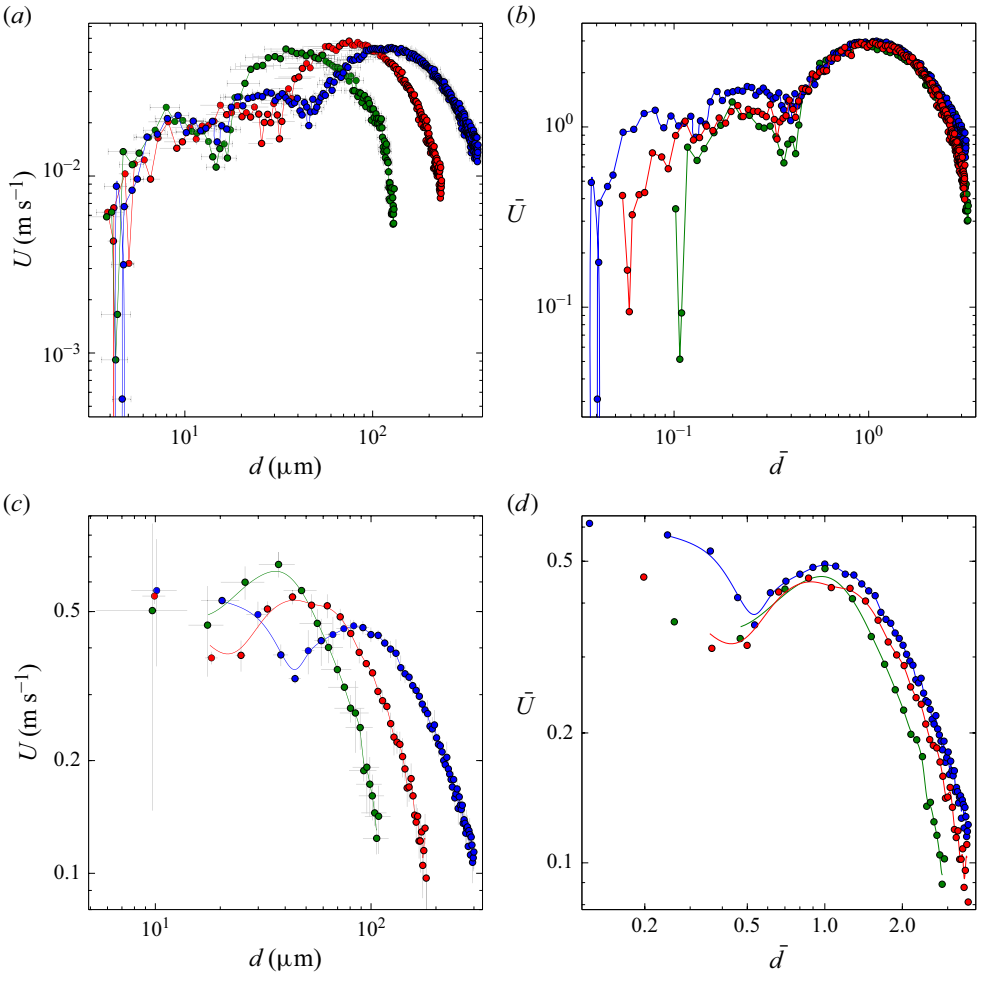

Figure 7. Influence of geometric constraints on the dynamic behaviour of the capillary bridge: breakup velocity versus minimum width for (*a*) the 70 % liquid and (*c*) the 0 % liquid. The error bars represent the standard deviation of at least four experiments. Scaled breakup velocity versus scaled minimum width for (*b*) 70 % and (*d*) the 0 % liquid. The legend of panel (*a*) applies to all panels.

formation of liquid bridges inside a highly viscous fluid. Tjahjadi *et al.* (1992) studied the formation of satellite and subsatellite droplets for such a case. Their results were expressed as a function of the viscosity ratio between the outer and inner liquid. Unlike free liquid bridges surrounded by an inviscid fluid, the liquid bridge undergoes tertiary, quaternary and higher-order necking. Since in most cases, tertiary and higher order neckings are absent for free liquid bridges surrounded by an invicid fluid, we speculate that the viscous drag force exerted by the outer fluid is responsible for this phenomenon. While the underlying physical mechanisms are different, the results of Tjahjadi *et al.* show a striking resemblance to our experimental images. We hypothesise that, with respect to the shape evolution of the liquid bridge and satellite formation, the contact-line forces act somewhat similarly to the drag forces by the outer viscous fluid.

For a wetting liquid bridge, the number of necks before breakup is a function of the surface properties as well as liquid viscosity. Analogous to a free liquid bridge surrounded

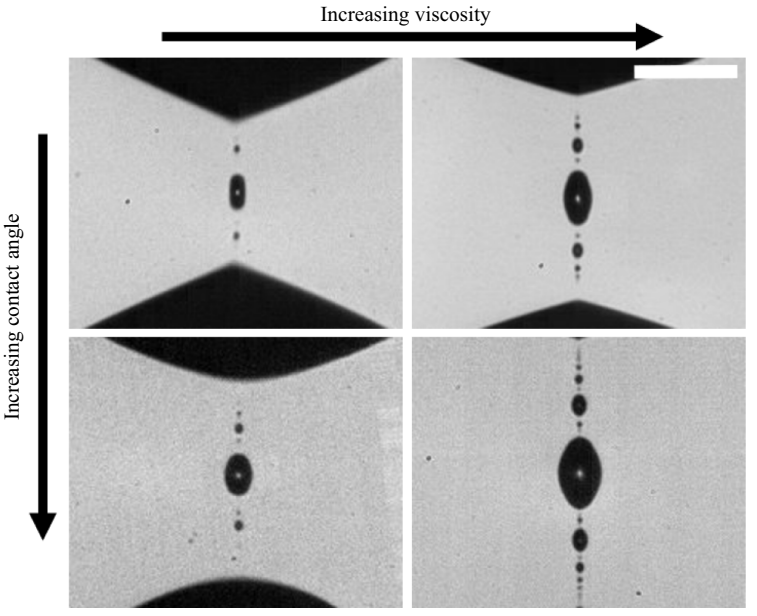

Figure 8. Change in number and shape of the satellite drops with viscosity and the contact angle of the substrate for wetting capillary bridges. The scale bar represents 100 μm.

by an inviscid fluid, the highly deformed shape is also observed for lower viscosities (see, e.g. the last frame showing the 0 % liquid in figure 4). However, unlike a free liquid bridge, the satellite droplet in the middle is larger for higher viscosities. Additionally, within the chosen parameter range in this study, longer capillary bridges – whether due to higher viscosity of the liquid or larger contact angle of the surface – produce more satellite droplets, as can be seen in figure 8. As mentioned earlier, many parameters of the surface influence the wetting behaviour and thus the breakup dynamics or the morphology of the satellite droplet. However, for the purpose of conciseness, here we only refer to the contact angle.

4. Conclusion

The breakup dynamics of viscous capillary bridges on solid surfaces was studied experimentally. It was shown that the surface properties play a significant role in the dynamics, as indicated by the fact that the breakup process is much faster for the PDMS@Au surface compared with the Au surface. The solid surface plays a twofold role. First, it slows down the dynamics of the capillary bridge through friction forces at the three-phase contact line. Contact-line friction is the dominant dissipation mechanism at small contact angles and low viscosities. Second, viscous dissipation at the surface away from the contact line plays a role. This contribution tends to become important with increasing liquid viscosity and contact angle.

In the experiments, the viscosity of the working liquids (water/glycerol mixtures) was systematically varied. As expected, the breakup velocity decreases with increasing viscosity. It was shown that the effects of molecular origin according to the MKT likely dominate over hydrodynamic dissipation in the liquid wedge. Furthermore, when the liquid bridge becomes very long, the viscous dissipation due to the axial flow also becomes substantial. To interpret the data, we introduced a total friction factor that incorporates the

effects of molecular origin according to the MKT, hydrodynamics in the liquid wedge and the viscous forces due to axial flow.

The most important quantity observed in the experiments on capillary bridge breakup is the minimum width of the bridge as a function of time. In the framework of the total friction force, a scaling model for the time dependence of the minimum width was formulated. The viability of this scaling is demonstrated by the fact that in the viscous regime, the curves showing the minimum width versus time collapse on the same master curve upon rescaling of the axes. Furthermore, the influence of external geometrical constraints on the breakup dynamics was studied. It was shown that changing the external length scale does not affect the maximum breakup velocity of the viscous capillary bridges. By contrast, for inertia-dominated capillary bridges, the maximum velocity increases as the size of the system decreases. It was hypothesised that the length scale governing the capillary breakup is the minimum width of the capillary bridge at the onset of instability. However, due to the difficulties in determining this value precisely, it was shown that the minimum width at the maximum velocity could serve as an equally viable length scale for the problem. This was confirmed by rescaling the axes in a diagram that shows the breakup velocity versus time for different external length scales.

Lastly, a qualitative assessment of the morphologies of the satellite droplets after capillary breakup revealed similarities and differences between free and wetting bridges. Similar to free liquid bridges, low viscosity wetting bridges experience a highly deformed shape before breakup. However, unlike free liquid bridges, wetting bridges with higher viscosity produce a larger satellite droplet in the middle. Increasing the contact angle on the surface and the liquid viscosity leads to longer bridges and more satellite droplets.

Acknowledgements. We express our gratitude to A.Erb for his invaluable assistance with the experimental part.

Funding. This study was funded by German Research Foundation (DFG) within the Collaborative Research Centre 1194 'Interaction of Transport and Wetting Processes,' Project-ID 265191195, subprojects A02a and A02b.

Declaration of interests. The authors report no conflict of interest.

References

Ambravaneswaran, B. & Basaran, O.A. 1999 Effects of insoluble surfactants on the nonlinear deformation and breakup of stretching liquid bridges. *Phys. Fluids* **11** (5), 997–1015.

Anthony, C.R. *et al.* 2023 Sharp interface methods for simulation and analysis of free surface flows with singularities: breakup and coalescence. *Annu. Rev. Fluid Mech.* **55** (1), 707–747.

Bewig, K.W. & Zisman, W.A. 1965 The wetting of gold and platinum by water. *J. Phys. Chem.* **69** (12), 4238–4242.

Bhat, P.P., Appathurai, S., Harris, M.T., Pasquali, M., McKinley, G.H. & Basaran, O.A. 2010 Formation of beads-on-a-string structures during break-up of viscoelastic filaments. *Nat. Phys.* **6** (8), 625–631.

Blake, T.D. & De Coninck, J. 2002 The influence of solid–liquid interactions on dynamic wetting. *Adv. Colloid Interface* **96** (1–3), 21–36.

Blake, T.D. 2006 The physics of moving wetting lines. *J. Colloid Interface Sci.* **299** (1), 1–13.

Bonn, D., Eggers, J., Indekeu, J., Meunier, J. & Rolley, E. 2009 Wetting and spreading. *Rev. Mod. Phys.* **81** (2), 739–805.

Brenner, M.P., Lister, J.R. & Stone, H.A. 1996 Pinching threads, singularities and the number 0.0304. . .. *Phys. Fluids* **8** (11), 2827–2836.

Castrejón-Pita, J.R., Castrejón-Pita, A.A., Thete, S.S., Sambath, K., Hutchings, I.M., Hinch, J., Lister, J.R. & Basaran, O.A. 2015 Plethora of transitions during breakup of liquid filaments. *Proc. Natl Acad. Sci. USA* **112** (15), 4582–4587.

Chen, H., Ponce-Torres, A., Montanero, J.M. & Amirfazli, A. 2021 Viscoelastic liquid bridge breakup and liquid transfer between two surfaces. *J. Colloid Interface Sci.* **582**, 1251–1256.

CHEN, Y.-J. & STEEN, P.H. 1997 Dynamics of inviscid capillary breakup: collapse and pinchoff of a film bridge. *J. Fluid Mech.* **341**, 245–267.
CRASTER, R.V., MATAR, O.K. & PAPAGEORGIOU, D.T. 2002 Pinchoff and satellite formation in surfactant covered viscous threads. *Phys. Fluids* **14** (4), 1364–1376.
DAVIS, S.H. 1980 Moving contact lines and rivulet instabilities. Part 1. The static rivulet. *J. Fluid Mech.* **98** (2), 225–242.
DAY, R.F., HINCH, E.J. & LISTER, J.R. 1998 Self-similar capillary pinchoff of an inviscid fluid. *Phys. Rev. Lett.* **80** (4), 704–707.
DE GENNES, P.G. 1985 Wetting: statics and dynamics. *Rev. Mod. Phys.* **57** (3), 827–863.
DIEZ, J.A., GONZÁLEZ, A.G. & KONDIC, L. 2009 On the breakup of fluid rivulets. *Phys. Fluids* **21** (8), 082105.
DIEZ, J.A. & KONDIC, L. 2007 On the breakup of fluid films of finite and infinite extent. *Phys. Fluids* **19** (7), 072107.
DUVIVIER, D., BLAKE, T.D. & DE CONINCK, J. 2013 Toward a predictive theory of wetting dynamics. *Langmuir* **29** (32), 10132–10140.
EGGERS, J. 1993 Universal pinching of 3D axisymmetric free-surface flow. *Phys. Rev. Lett.* **71** (21), 3458–3460.
EGGERS, J. 2005 Drop formation – an overview. *Z. Angew. Math. Mech.* **85** (6), 400–410.
EGGERS, J. 2012 Stability of a viscous pinching thread. *Phys. Fluids* **24** (7), 036601.
EGGERS, J. & VILLERMAUX, E. 2008 Physics of liquid jets. *Rep. Prog. Phys.* **71** (3), 036601.
EIFERT, A., PAULSSEN, D., VARANAKKOTTU, S.N., BAIER, T. & HARDT, S. 2014 Simple fabrication of robust water-repellent surfaces with low contact-angle hysteresis based on impregnation. *Adv. Mater. Interfaces* **1** (3), 1300138.
EL MOGY, T. 2021 An overview of 3D printing technology effect on improving solar photovoltaic systems efficiency of renewable energy. *Proc. Intl Acad. Ecol. Environ. Sci.* **11** (2), 52.
GRINFELD, M. 1994 On the Plateau–Rayleigh instability of truncated cylinder. *Mech. Res. Commun.* **21** (6), 613–616.
HARTMANN, M., FRICKE, M., WEIMAR, L., GRÜNDING, D., MARIĆ, T., BOTHE, D. & HARDT, S. 2021 Breakup dynamics of capillary bridges on hydrophobic stripes. *Intl J. Multiphase Flow* **140**, 103582.
HARTMANN, M. & HARDT, S. 2019 Stability of evaporating droplets on chemically patterned surfaces. *Langmuir* **35** (14), 4868–4875.
HUH, C. & SCRIVEN, L.E. 1971 Hydrodynamic model of steady movement of a solid/liquid/fluid contact line. *J. Colloid Interface Sci.* **35** (1), 85–101.
JENSEN, K.E., SARFATI, R., STYLE, R.W., BOLTYANSKIY, R., CHAKRABARTI, A., CHAUDHURY, M.K. & DUFRESNE, E.R. 2015 Wetting and phase separation in soft adhesion. *Proc. Natl Acad. Sci. USA* **112** (47), 14490–14494.
KAMAT, P.M., WAGONER, B.W., THETE, S.S. & BASARAN, O.A. 2018 Role of Marangoni stress during breakup of surfactant-covered liquid threads: reduced rates of thinning and microthread cascades. *Phys. Rev. Fluids* **3** (4), 043602.
KANG, B.J., LEE, C.K. & OH, J.H. 2012 All-inkjet-printed electrical components and circuit fabrication on a plastic substrate. *Microelectron. Engng* **97**, 251–254.
KAWAMOTO, H. 2007 Electronic circuit printing, 3D printing and film formation utilizing electrostatic inkjet technology. In *NIP & Digital Fabrication Conference*, vol. 23, pp. 961–964. Society of Imaging Science and Technology.
KING, J.R., MÜNCH, A. & WAGNER, B. 2006 Linear stability of a ridge. *Nonlinearity* **19** (12), 2813–2831.
KUMAR, S. 2015 Liquid transfer in printing processes: liquid bridges with moving contact lines. *Annu. Rev. Fluid Mech.* **47** (1), 67–94.
LI, X. *et al.* 2022 Spontaneous charging affects the motion of sliding drops. *Nat. Phys.* **18** (6), 713–719.
LI, X., RATSCHOW, A.D., HARDT, S. & BUTT, H.-J. 2023 Surface charge deposition by moving drops reduces contact angles. *Phys. Rev. Lett.* **131** (22), 228201.
LI, Y. & SPRITTLES, J.E. 2016 Capillary breakup of a liquid bridge: identifying regimes and transitions. *J. Fluid Mech.* **797**, 29–59.
LIAO , Y.-C., FRANSES , E.I. & BASARAN , O.A. 2006 Deformation and breakup of a stretching liquid bridge covered with an insoluble surfactant monolayer. *Phys. Fluids* **18** (2), 022101.
LIN, S.-P. 2003 *Breakup of Liquid Sheets and Jets*. Cambridge University Press.
MARTÍNEZ-CALVO, A., RIVERO-RODRÍGUEZ, J., SCHEID, B. & SEVILLA, A. 2020 Natural break-up and satellite formation regimes of surfactant-laden liquid threads. *J. Fluid Mech.* **883**, A35.
MCGOUGH, P.T. & BASARAN, O.A. 2006 Repeated formation of fluid threads in breakup of a surfactant-covered jet. *Phys. Rev. Lett.* **96** (5), 054502.

PAN, X., HU, M., XU, B., WANG, F., HUO, P., CHEN, F., GU, Z. & DENG, D. 2021 Armstrong liquid bridge: formation, evolution and breakup. *Phys Rev. Fluids* **6** (9), 093901.

PAPAGEORGIOU, D.T. 1995*a* Analytical description of the breakup of liquid jets. *J. Fluid Mech.* **301**, 109–132.

PAPAGEORGIOU, D.T. 1995*b* On the breakup of viscous liquid threads. *Phys. Fluids* **7** (7), 1529–1544.

PESCHKA, D., HAEFNER, S., MARQUANT, L., JACOBS, K., MÜNCH, A. & WAGNER, B. 2019 Signatures of slip in dewetting polymer films. *Proc. Natl Acad. Sci. USA* **116** (19), 9275–9284.

PONCE-TORRES, A., RUBIO, M., HERRADA, M.A., EGGERS, J. & MONTANERO, J.M. 2020 Influence of the surface viscous stress on the pinch-off of free surfaces loaded with nearly-inviscid surfactants. *Sci. Rep.* **10** (1), 16065.

RATSCHOW, A.D., BAUER , L.S., BISTA , P., WEBER , S.A. L., BUTT , H.-J. & HARDT , S. 2024 How charges separate when surfaces are dewetted. *Phys. Rev. Lett.* **132** (22), 224002.

ROSTAMI P., HORMOZI M.A., SOLTWEDEL O., AZIZMALAYERI R., VON KLITZING R. & AUERNHAMMER G.C. 2023 Dynamic wetting properties of PDMS pseudo-brushes: four-phase contact point dynamics case. *J. Chem. Phys.* **158** (19), 194703.

RUBIO, M., PONCE-TORRES, A., HERRADA, M.A., GAÑÁN-CALVO, A.M. & MONTANERO, J.M. 2021 Effect of an axial electric field on the breakup of a leaky-dielectric liquid filament. *Phys. Fluids* **33** (9), 092114.

TAKAMURA, K., FISCHER, H. & MORROW, N.R. 2012 Physical properties of aqueous glycerol solutions. *J. Petrol. Sci. Engng* **98**, 50–60.

TIMMERMANS, M.L. & LISTER, J. 2002 The effect of surfactant on the stability of a liquid thread. *J. Fluid Mech.* **459**, 289–306.

TING, L. & KELLER, J.B. 1990 Slender jets and thin sheets with surface tension. *SIAM J. Appl. Maths* **50** (6), 1533–1546.

TJAHJADI, M., STONE, H.A. & OTTINO, J.M. 1992 Satellite and subsatellite formation in capillary breakup. *J. Fluid Mech.* **243**, 297–317.

TOMOTIKA, S. 1935 On the instability of a cylindrical thread of a viscous liquid surrounded by another viscous fluid. *Proc. R. Soc. Lond. A-Math. Phys. Sci.* **150** (870), 322–337.

TOWNE, S., VISWANATHAN, V., HOLBERY, J. & RIEKE, P. 2007 Fabrication of polymer electrolyte membrane fuel cell meas utilizing inkjet print technology. *J. Power Sources* **171** (2), 575–584.

TRUJILLO-PINO, A.D., KRISSIAN, K., ALEMÁN-FLORES, M. & SANTANA-CEDRÉS, D. 2013 Accurate subpixel edge location based on partial area effect. *Image Vision Comput.* **31** (1), 72–90.

VOINOV, O.V. 1976 Hydrodynamics of wetting. *Fluid Dyn.* **11** (5), 714–721.

VOINOV, O.V. 2000 Wetting line dynamics in the process of drop spreading. *J. Colloid Interface Sci.* **226** (1), 22–28.

WANG, Y., GUO, H., CHEN, J.-J., SOWADE, E., WANG, Y., LIANG, K., MARCUS, K., BAUMANN, R.R. & FENG, Z.-S. 2016 Based inkjet-printed flexible electronic circuits. *ACS Appl. Mater. Interfaces* **8** (39), 26112–26118.

WEE, H., WAGONER, B.W., KAMAT, P.M. & BASARAN, O.A. 2020 Effects of surface viscosity on breakup of viscous threads. *Phys. Rev. Lett.* **124** (20), 204501.

WHITE, M.L. 1964 The wetting of gold surfaces by water. *J. Phys. Chem.* **68** (10), 3083–3085.